Pergamon

Int. J. Heat Mass Transfer. Vol. 40, No. 8, pp. 1807–1815, 1997

0017–9310/97 $17.00+0.00

PII: S0017–9310(96)00258–X

Heat-transfer and defrosting characteristics of a horizontal array of cooled tubes immersed in a very shallow fluidized bed

TOSHIO AIHARA, TAKU OHARA, TOSHIYUKI SHIMOYAMA and HITOSHI KITANO†

Institute of Fluid Science, Tohoku University, 2-1-1 Katahira, Aoba-ku, Sendai 980-77, Japan

(*Received* 10 *November* 1995 *and in final form* 9 *July* 1996)

Abstract—Heat transfer and defrosting characteristics of a horizontal single-row array of cooled tubes immersed in a gas-solid fluidized bed, have been studied experimentally. The fluidized bed produces gas-solid particle impinging jets to effectively remove frost layers on the tube surface. It has been verified that frost-free running of the cooled tubes is possible under the conditions of inlet air temperature −7°C, tube-surface temperature −17°C and relative humidity 80%. The local contact frequency of particles onto the tube surface was measured by an optical sensing system and the defrosting mechanism of impinging solid particles was observed in detail with a visualization technique.

1. INTRODUCTION

In the cases where conventional finned tube heat exchangers are used as evaporators in heat pump systems and LNG-gasification systems, the moisture in humid air freezes and a thick frost layer forms on the fin surfaces. The frost layer reduces the heat transfer, increases the pressure loss, and finally results in choking of the evaporators.

Hence, a number of research works on the frosting mechanism and heat transfer have been carried out [1–4]. The present authors have also clarified the effect of increasing thermal resistance and latent-heat release due to frosting on the transient heat-transfer characteristics of horizontal cold tube banks, exposed to impinging jets [5].

A promising solution to this problem is to immerse the cold tubes in a fluidized bed and to utilize solid-particle impingement onto the frost layers. By this technique, we can expect both effective defrosting and heat-transfer augmentation due to the latent-heat release in frosting.

However, a conventional bubbling-type fluidized bed with a comparatively large static bed height [6–15] produces a very high pressure loss, though it shows excellent performance in heat-transfer and defrosting of tubes [16, 17]. Hence, one of the present authors developed a very shallow fluidized-bed heat exchanger, which was composed of a horizontal tube array and a specially designed multislit distributor producing a gas/solid-particle jet impinging onto each tube [18–20]. This very shallow fluidized bed, despite its very small static bed height, showed a heat transfer performance comparable to that of a bubbling-type fluidized bed, while its pressure loss was extremely small. Also performed was an extensive cooling test of the single-array of cooled tubes, 10 mm in diameter, immersed in the very shallow fluidized bed. It was verified that continuous frost-free running of long duration is possible even under the thermal conditions where the whole cold tube surfaces are covered with thick frost layers when they are placed in single-phase gas flow [21].

In the present study, defrosting experiments were carried out using an improved cornice-type distributor, instead of the flat multislit distributor used in the previous study [21], together with an array of larger tubes (20 mm in diameter). Then the transient local heat-transfer coefficients were measured and the defrosting mechanisms were investigated by two newly developed techniques: optical measurement of local contact frequency of solid particles onto the tube surface; visual observation from inside of the tube on the frost formation and defrosting by particle impingement. By the use of the present defrosting system, continuous frost-free running was possible under the experimental conditions, even in the case of a tube temperature as low as −17°C.

2. EXPERIMENTAL APPARATUS AND PROCEDURE

2.1. *Test fluidized bed*

The test wind tunnel has controlling sections of the temperature, θ_{ai}, and relative humidity, ϕ_{ai}, of air flowing into the test section. The details of the wind

† Currently with Idemitsu Co Ltd, Japan.

NOMENCLATURE

d_p	average diameter of particles
d_t	diameter of test tube
f_c	contact frequency of particles onto tube surface
h	total heat-transfer coefficient, equation (1)
$\dot{q}_w$	heat flux at the surface of test tube
T	Kelvin temperature
t	time after the beginning of a cooling run
u_{fr}	superficial air velocity.

Greek symbols

β	azimuthal angle, measured from the forward stagnation point
θ	Celsius temperature
ξ	frosted area fraction
ν_a	kinematic viscosity of air
ϕ_{ai}	relative humidity of inlet air
χ	absolute humidity of inlet air.

Subscripts

ai	inlet air
mi	inlet methanol
w	tube surface
β	local value at a location of angle β.

Superscript

	average over the circumference.

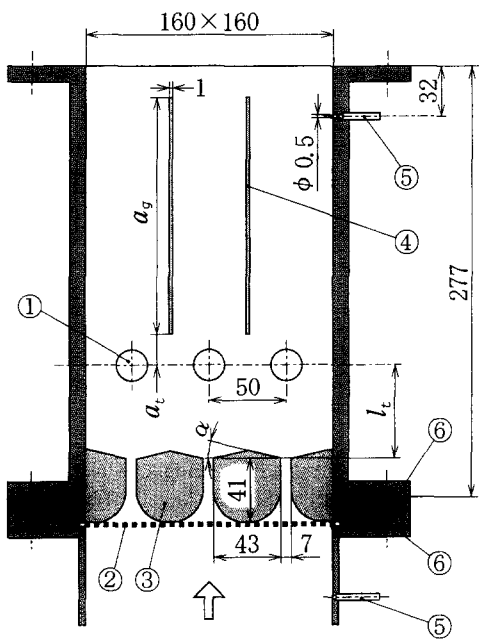

Fig. 1. Outline of test section (dimensions are in mm).

tunnel are given in our previous report [21]. Figure 1 illustrates the outline of the test section, which is composed of an acrylic resin duct of 160 mm × 160 mm and a multislit distributor (3). In the present experiment, a new cornice-type distributor was used as shown in Fig. 1. The reason for this is that, although a flat-type distributor of a plate having many parallel slits was used in the previous study [21], the solid particles had the tendency to deposit on a stagnant zone between the neighbouring slits, and to destabilize the jet flow from the distributor.

The slit nozzles were located just below the respective tubes to produce gas-particle impinging jets. The opening ratio, defined as the total opening area of slit nozzles divided by the frontal area of the duct, was determined to be 13% so as to obtain the best defrosting effect. The inlet ports of the distributor were covered with a wire net (2) of 20 meshes to store the particles. Guiding plates (4) were used to stabilize fluidization. White spherical glass beads of the geometrical mean diameter $d_p = 1.54$ mm, screened with two standard sieves having the mesh sizes of 1.68 and 1.41 mm, were used.

In a cooling run, the test tubes (1) were cooled down to $\theta_w = -20°C$ with cold methanol as a coolant. In the heating run, the test tubes were heated up to 70°C using hot water.

2.2. *Test tube*

The body of the test tube was made of duralumin, as shown in Fig. 2. The outer and inner diameters of the tube were 19 and 7 mm, respectively; its outer surface was coated with a Teflon film so as to have the final diameter of 20.0 mm. Measurements of the principal parameters, such as temperature and heat flux at the tube surface, were made on the middle one of the three tubes installed in the test duct. Twelve staggered shallow grooves were machined in the body surface at every 30° in the middle of its length and thin film heat-flow sensors were attached to these arc-shaped grooves with conducting adhesives as shown in Fig. 2. All the gaps were filled with conducting silver paint. The local wall heat-flux, $\dot{q}_{w,\beta}$, was measured with the heat-flow sensors.

The local surface temperature of the test tube $\theta_{w,\beta}$ was estimated from the output of a T-type thermocouple set in each heat-flow sensor with correction

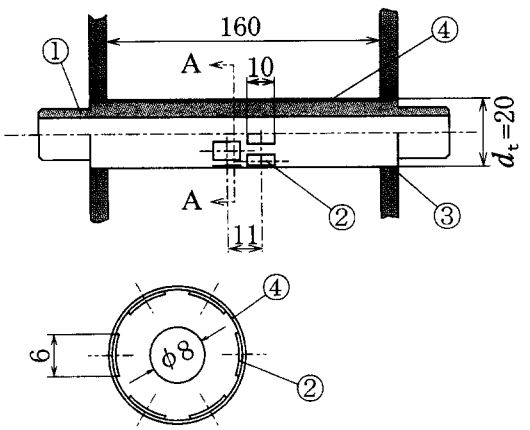

Fig. 2. Details of the test tube (dimensions are in mm).

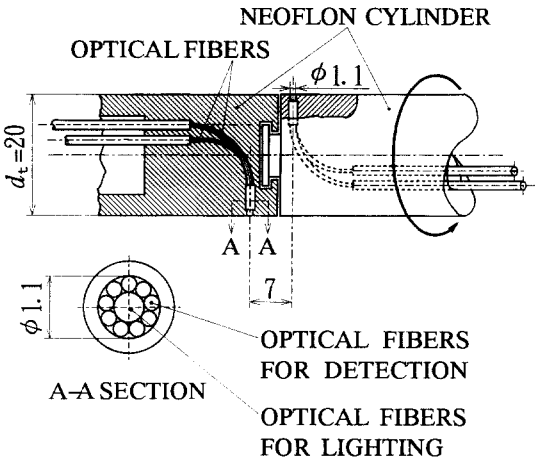

Fig. 3. Test tube for measuring particle contact frequency (dimensions are in mm).

considering the $\dot{q}_{w,\beta}$ and thermal resistances across the sensor, conducting paint, and Teflon film. Thus, the local heat-transfer coefficient h_β at an azimuthal angle β from the forward stagnation point is defined as

$$h_\beta = \dot{q}_{w,\beta}/(\theta_{ai} - \theta_{w,\beta}). \quad (1)$$

Here, h_β is the total heat-transfer coefficient, including the effect of both the thermal resistance of frost layer on the tube surface and the latent-heat release during frost formation.

The bulk temperature of the coolant was measured by a thermopile consisting of five K-type couples installed in both mixers at the inlet and outlet ports of the test tube.

2.3. *Measurement of particle contact frequency*

Several techniques have been applied to detect the frequency of particles approaching a tube surface in a fluidized bed. One is a transmitted-light type optical sensing system [12, 15, 22] with a couple of optical fibers for lighting and detecting, opposing each other. In another technique, lighting was adjusted to satisfy the condition of total reflection at the observation surface; the instantaneous loss of total reflection by contact of a particle to the surface were utilized [14]. An electrostatic capacitance probe has also been applied [23].

In the present experiment, a new optical sensing system of reflected-light type was used. In the system, the optical probes were buried in the tube surface as shown in Fig. 3. The merits of this method are as follows: (i) a particle approaching a measuring point at the tube surface can be detected individually; (ii) the optical system is protected from the impingement of high-speed particles; (iii) the measuring system never disturbs the motion of fluidizing particles. As shown in Fig. 3, cross section A–A, the lighting fibers were surrounded by a large number of detecting fibers; the respective terminal ends of a couple of the optical fiber bundles were installed at the surface of a Neoflon cylinder 20 mm in outer diameter. Red light-emitting diodes and photodetectors were connected to the other ends of these optical fibers that were separated outside the test tube. The present lighting-detecting system was able to detect a particle entering the sensing area by the light reflected from the particle. Electric signals from the photodetector were amplified and converted to binary, 0 or 5 V; the square wave signals were inputted to a counter board on a personal computer and the number of particle entries into the sensing area was counted. The response frequency of the present system was approximately 60 kHz, which was sufficiently high in comparison with the measured contact frequencies (30 Hz maximum).

The size of the sensing area was adjustable in the process of amplification and binary-conversion of the electric signals. For example, an increase in the threshold value at binary-conversion or amplification degree enables the system to detect weaker reflected light from a particle at a longer distance; thus the sensing area is enlarged. At the present measurement, the size of the sensing area was determined to be sufficiently small as to eliminate the detection of particles entering the sensing area but passing-by without any contact to the tube surface. Figure 4 shows the sensing area of the present optical system, which is approximately a hemi-sphere of a radius 0.5 mm from the detecting hole. A sensing area smaller than the present one made the detection of contact particles unstable—the present sensing area gave the best results. Since the radius of the sensing area was approximately 1/3 of the mean particle diameter d_p = 1.54 mm, the present system had sufficient measuring accuracy.

As shown in Fig. 3, the test tube was divided into two pieces in the axial direction; one was fixed and

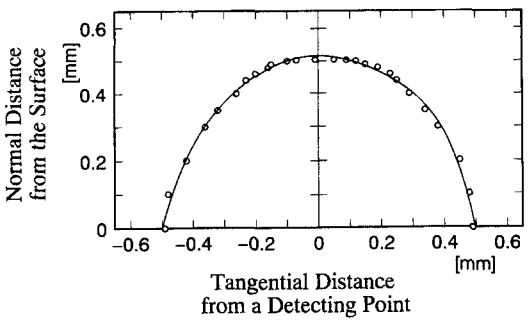

Fig. 4. Sensing area of the optical system.

the other freely rotatable. The fixed sensor always measured the contact frequency at the forward stagnation point, while the rotatable sensor simultaneously measured the local contact frequency at the arbitrary azimuthal angle.

In the experiment measuring contact frequency, the middle one of the three tubes shown in Fig. 1 was replaced by the above-mentioned Neoflon cylinder with optical probes, and a fluidizing run was performed under an isothermal condition.

2.4. *Observation equipment for defrosting mechanism*

In the present experiment, we successfully observed the frost formation and defrosting by particle impingement on the cooled tube surface from inside the tube using a video camera†. The observation equipment, composed of double Pyrex tubes, is shown in Fig. 5. The outer diameter and thickness of the outer tube were 19 and 1.2 mm, respectively; those of the inner tube were 12 and 1.0 mm, respectively. The outer tube was coated with a thin Teflon film so as to have a final diameter of 20 mm. The coaxial double tubes were cooled with cold methanol flowing between them so that the surface temperature might be almost uniform. Illumination of the outer surface was made by lighting with a beam splitter (1) and a 45° inclined mirror (2); the frosting and defrosting behavior was observed by a video camera from the outside and recorded. For the lighting, a stroboscope was utilized to obtain a clear still image. It was possible to move the mirror (2) in an axial direction and rotate it in order to observe the behavior of frost layer at an arbitrary axial and angular location. The pressure in the inner tube was reduced to 10^{-3} torr with a vacuum pump to prevent the inner surface from condensation and frost formation.

In the observation experiment, the middle one of the three tubes shown in Fig. 1 was replaced by the above-mentioned equipment, and a cooling run was performed.

† Observation from the inside of a tube on the behavior of fluidizing particles under isothermal conditions has been reported by Kurosaki *et al.* [12] and Ishiguro *et al.* [13, 15].

3. EXPERIMENTAL RESULTS AND DISCUSSION

3.1. *Optimum fluidizing conditions and test temperatures*

The optimum operating conditions giving stable fluidization and high particle number-density around the test tubes were examined by a preliminary experiment varying the pertinent parameters in a wide range; namely, the inclination angle of the distributor $\alpha = 0.23$ or 0.31 rad; the distance from the jet nozzle to the test tube $l_t = 20$–80 mm; the equivalent static bed height per frontal area, $l_0 = 5$–20 mm, corresponding to the ratio of the packed volume of glass beads to the frontal area; the distance from the test tube to the lower edge of the guiding plates $a_t = 0$–200 mm; the length of the guiding plates $a_g = 0$–300 mm; the superficial air velocity $u_{fr} = 2.6$–4.8 m s^{-1} (for the symbols see Fig. 1). Then, the optimum conditions were found as follows: $\alpha = 0.23$ rad, $l_t = 60$ mm, $l_o = 10$ mm, $a_t = 20$ mm, $a_g = 150$ mm, and $u_{fr} = 3.2$ m s^{-1}. Every experiment in the present study was made under these conditions.

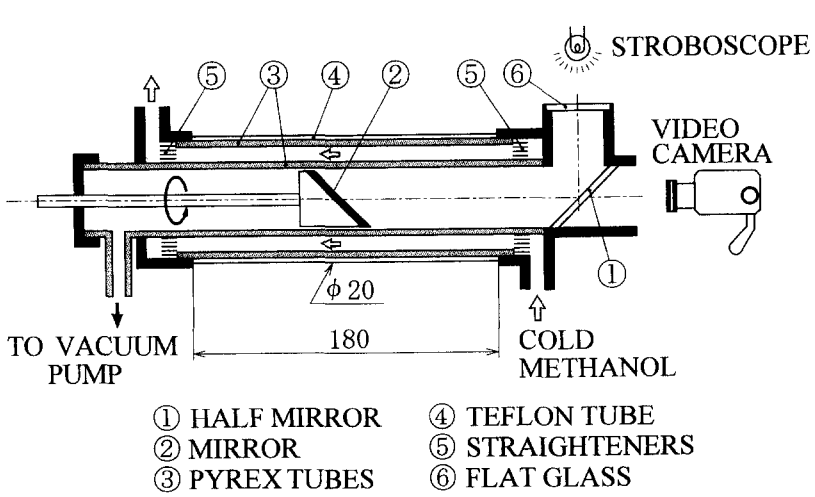

Fig. 5. Cooled test tube for the observation of the defrosting process (dimensions are in mm).

Table 1. Experimental conditions

θ_{ai} (°C)	θ_{mi} (°C)		
+5	−15	−20	−25
−1	—	−17	−27
−7	—	−17	−27

The thermal conditions for the present experiment were as follows: in the heating test, inlet air temperature $\theta_{ai} = 5$°C and inlet temperature of hot water 20°C; two cooling tests were carried out at the air temperatures θ_{ai} and inlet methanol temperature θ_{mi} listed in Table 1. The relative humidity of the inlet air ϕ_{ai} was maintained to be 80% in every test.

3.2. *Defrosting characteristics*

3.2.1. *Contact frequency of particles.* Figure 6 shows the circumferential distribution of the local contact frequency, $f_{c,\beta}$, of particles onto the tube surface. In this figure, $f_{c,o}$ denotes the contact frequency at the stagnation point $\beta = 0$. Counting of particle contacts during 100 s was repeated 10 times at each azimuthal angle β, and the average values are plotted in the figure where the standard deviations $\pm S_f$ of measured values are also indicated.

The average value of $f_{c,o}$ is approximately 5×10^6 $m^{-2}\,s^{-1}$, which is in excellent agreement with a theoretical prediction based on an analysis of the gas-solid particle impinging jet formed in the present fluidized bed [24].

As the angle β is increased, the values of $f_{c,\beta}$ become smaller than the value at the stagnation point, $f_{c,o}$. This results from impingement of low-speed particles which deviate from the jet center into the shear layer. Although the impinging velocity of particles continues to decrease with increasing $|\beta|$, the rate of the particles sliding or rolling on the tube surface without rebounding increases with $|\beta|$, as shown below. Therefore, $f_{c,\beta}$ increases rapidly as $|\beta|$ exceeds about $\pi/6$. On the upper half surface of the tube ($|\beta| > \pi/2$), the fluidized particles are falling down to that point. Since these were also counted, $f_{c,\beta}$ shows maximum value at $|\beta| \simeq \pi/2$. In the region of $|\beta| > \pi/2$, the effect of the gas-solid impinging jet weakens rapidly, though there is a weak Coanda effect. Consequently, the value of $f_{c,\beta}$ decreases again and reaches its minimum at $|\beta| \simeq \pi$.

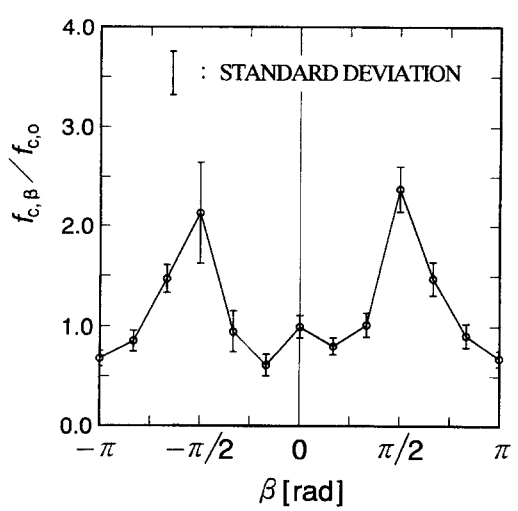

Fig. 6. Local contact frequency of particles onto the test tube surface.

3.2.2. *Observation of the defrosting mechanism.* Figure 7 shows typical still pictures† reproduced from the video movies of the defrosting process, which were recorded by the method described in Section 3.4. Photographs (a)–(d) were taken at 18–27 min after the start of cooling under the conditions of $\theta_{ai} = 4.7$°C and $\theta_w \simeq -0.6$°C ± 0.2°C. The frost was soft in the early stage and was easily removed by impingement or sliding of solid particles; accordingly, the traces of particle motion on the tube surface are visualized as dark spots (impingement marks) and dark lines (scraping marks) in the white frost layer. The bright line appearing at the center of view resulted from the reflection of illumination at the inner surface of the inner tube; the direction of the bright line corresponds to the axis of the test tube. The angular size of the visual field including the bright line was $\pi/3$.

Around the stagnation point ($\beta = 0$), most particles impinge almost normal to the tube and rebound away from it, as can be seen from the numerous impingement marks in picture (a) of Fig. 7. The rate of sliding particles increases as $|\beta|$ exceeds about $\pi/4$ (see picture (b)), and scraping marks are observed much more frequently than impingement marks at $|\beta| \simeq \pi/2$ (see picture (c)). There are a lot of particles sliding axially and also some particles marking a loop on the tube surface; the length of the scraping marks frequently reaches 4–5 mm. It can be seen from these marks that a complicated motion of particles exists near the tube surface. Near the top of the tube, the impingement marks increase again due to particles falling from the upper area of the bed, though being hardly distinguishable from a large number of scraping marks in the still picture (d). Picture (e) shows a complete frost-free state achieved by defrosting.‡

Pictures (f) and (g) show the defrosting process with a thicker frost layer, which was observed at 39 and 42 min, respectively, after the start of cooling under the conditions of $\theta_{ai} = 4.9$°C and $\theta_w \simeq -2.2$°C ± 0.1°C. In this case, the frost layer becomes dense and hard owing to particle impingement, and begins to be scaled off in the form of a small piece from the tube surface in a short time. At a much lower tube-temperature, the frost layer sticks faster to the tube surface; accordingly, the frost layer is scaled

† The resolution of these still pictures is not so good as in the video movies, because of technical limitations of the video recording system.

‡ Particles are not seen as spherical because of the optical deformation owing to observation through the cylindrical test-tube walls.

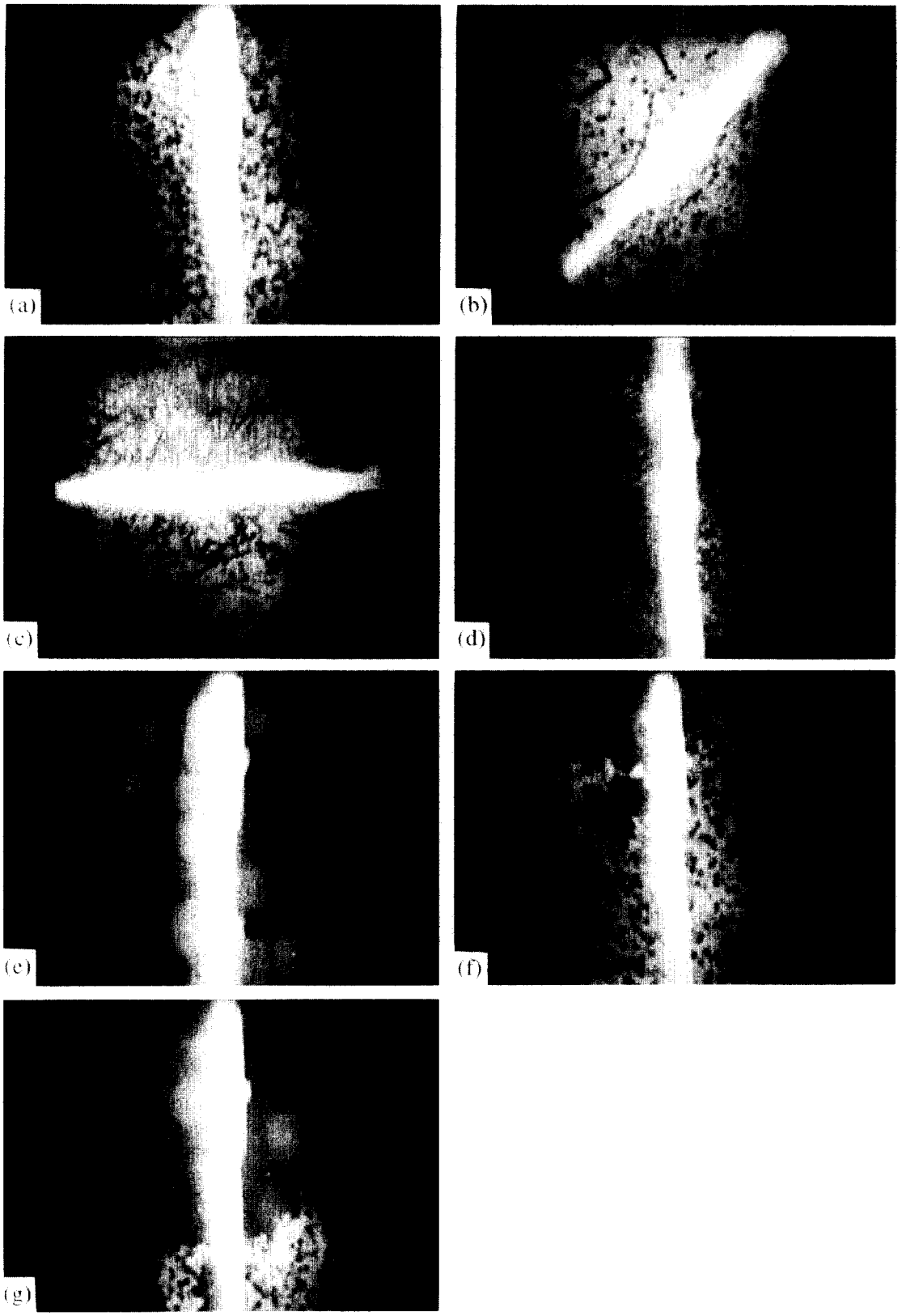

Fig. 7. Still pictures of the defrosting process, reproduced from video movies. (a) $\beta = 0$; (b) $\beta = \pi/4$; (c) $\beta = \pi/2$; (d) $\beta = \pi$; (e) completely frost-free state, $\beta = 0$; (f) defrosting process, $\beta = 0$, $t = 39$ min; (g) defrosting process, $\beta = 0$, $t = 42$ min.

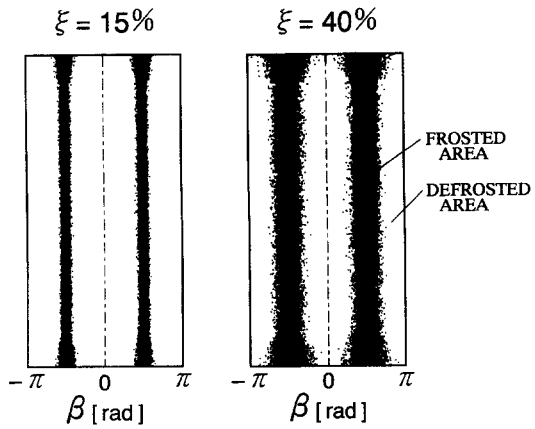

Fig. 8. Frost patterns on the tube surface.

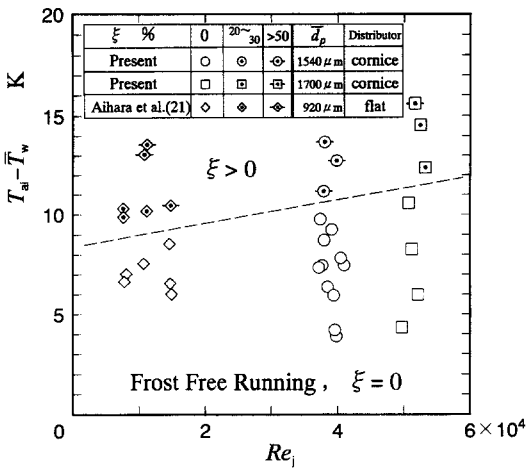

Fig. 9. Defrosting limit of the cooled tube immersed in the very shallow fluidized bed.

off only by the particle impingement near $\beta = 0$ or π, which is almost perpendicular to the tube surface, and the defrosting is hardly attained by sliding particles near $\beta \simeq \pi/2$.

3.2.3. *Frosted area fraction.* Here the frosted area fraction ξ is defined as the ratio of the frosted area to the total area of the test tube surface. The frosted area fraction ξ was determined by visual observation of the middle part of the test tube on a length of 80 mm, excluding both end parts within 40 mm from the duct walls in order to eliminate the end effect.

In the case of the same value of ξ, similar frosted patterns were observed, regardless of the running conditions of θ_{ai}, θ_{mi} and so on. The sketched frost patterns for $\xi = 15$ and 40% are shown in Fig. 8. As may be seen from the figure, the top ($|\beta| \simeq 0$) and bottom ($|\beta| \simeq \pi$ rad) surface of the tube have been defrosted effectively by the above-mentioned mechanism, in spite of running under the thermal condition where the whole tube surface would be completely frosted without particle impingement. However, the defrosting is not sufficient on the side surfaces near $\beta = \pi/2$. The more severe the cooling conditions, the thicker becomes the frost layer near $\beta = \pi/2$; then, the frosted area extends from the tube sides ($|\beta| \simeq \pi/2$) to the stagnation points ($|\beta| \simeq 0$ and π). This is mainly due to the change in the frost structure and an increase in frost formation.

3.2.4. *Defrosting limit.* The defrosting limit of the cooled tube immersed in the very shallow fluidized bed is shown in Fig. 9. In this figure, the results of an experiment using glass beads of $d_p = 1.7$ mm (the optimum fluidization velocity $u_{fr} = 4.2$ m s^{-1}) in the present apparatus and previous defrosting data for glass beads of $d_p = 0.92$ mm and a test tube of $d_t = 10$ mm [21] are also plotted along with the present data for glass beads of $d_p = 1.54$ mm. When the frosted area fraction ξ is plotted against the temperature difference ($T_{ai} - \bar{T}_w$) and the jet Reynolds number Re_j, the border line between the domains of frosting and frost-free running is quite clear, as can be seen in the figure, where the line of defrosting limit is indicated by a broken line. Continuous frost-free running is possible under the condition of $T_{ai} - \bar{T}_w < 10$ K regardless of the inlet air temperature, though the defrosting limit slightly increases with increasing Re_j. It should be noted that continuous frost-free running was still possible even in the case of a tube-surface temperature as low as -17°C, with the inlet air temperature being $\theta_{ai} = -7$°C.

3.3. *Defrosting heat-transfer characteristics*

Before performing the fluidized-bed experiments, a single-phase heat transfer experiment on impinging jet without glass beads has also been performed in the test apparatus with heated tubes. The measured local heat-transfer coefficients [5] was in good agreement with those by Kumada *et al.* [25, 26]; hence, the adequacy of the present experimental apparatus and measuring system has been verified.

Time histories of the local heat-transfer coefficients h_β are shown in Fig. 10 for $\beta = 0$ and π and $\theta_{ai} = 5$°C.

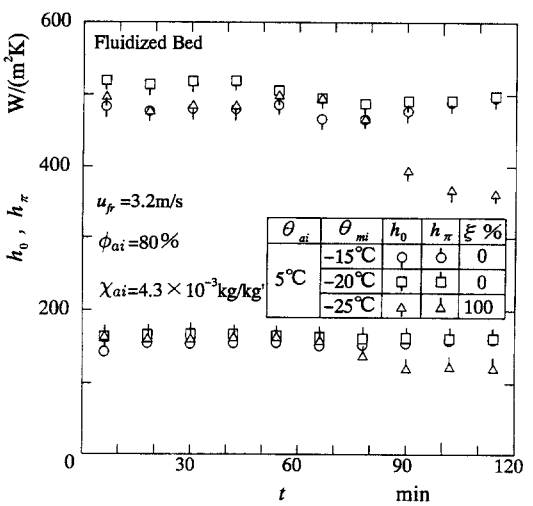

Fig. 10. Time histories of the local heat-transfer coefficient.

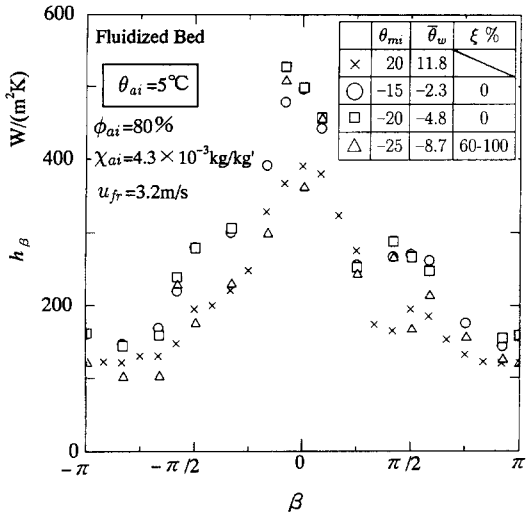

Fig. 11. Distribution of the local heat-transfer coefficient.

The measured values of ξ are also indicated in the figure.

In the cases of $\theta_{mi} = -15$°C and -20°C, frost crystals growing on the cold surface are immediately scraped off by particle impingement, and then the completely frost-free running is maintained. Consequently, the values of h_0 and h_π are kept constant during the cooling test, while in the case of $\theta_{mi} = -25$°C, the values of h_0 and h_π decrease with frost layer growth after $t \simeq 60$ min. When the whole tube surface was covered with the frost layer at $t = 120$ min, the decrease in the heat-transfer coefficients was approximately 25%.

Figure 11 shows a typical distribution of the local heat-transfer coefficient h_β measured at 2 h after the start of defrosting, when the thermal steady state has been attained. In the figure, the data obtained from heating test are also plotted. As to the case of $\theta_{mi} = -25$°C, the values of h_β measured for both $\xi = 60$ and 100% in two cooling runs are plotted in the figure. In the cases of $\theta_{mi} = -15$°C and -20°C, in which the frost-free state ($\xi = 0$) was maintained, the heat-transfer coefficients are higher than those for the heating test. This results from the following mechanism: fine frost crystals are scraped off from the tube surface by impinging particles; the crystals are segregated from the glass beads by the sizing action of the fluidized bed itself and are then discharged steadily from the bed. Thus, the defrosting heat-transfer is enhanced by the reasons that no thermal resistance layer is formed by defrosting, while utilizing the latent-heat release in frost formation. The mechanism described above is also supported by the fact that the heat-transfer coefficients are reduced considerably in the frosting case with $\theta_{mi} = -25$°C.

It should be added that a similar tendency was also obtained under the condition of $\theta_{ai} = -7$–5°C and that the large scatter of heat-transfer data in frosting depends upon the frosted state near the stagnation point ($\beta = 0$), which was different in each run.

4. CONCLUDING REMARKS

A very shallow fluidized bed, producing stable fluidization and effective defrosting characteristics, has been developed using a newly designed cornice-type distributor and large size particles. Heat-transfer and defrosting characteristics have been studied experimentally on an array of cooled tubes immersed in the fluidized bed. The obtained results are summarized as follows.

(1) The contact frequency of fluidizing particles at the tube surface was measured by an optical technique, and it was found that the contact frequency is low at the stagnation points ($\beta = 0$ and π) while it has a maximum near the tube sides ($\beta \simeq \pi/2$).

(2) The defrosting mechanism by particle impingement was visually observed from the inside of a specially designed cold tube. It is clarified that the defrosting is primarily done by particles impinging perpendicularly onto the tube surface near the forward stagnation point, by sliding particles on the tube sides, and by impinging and sliding particles around the top of tube ($\beta \simeq \pi$). Therefore, substantial discussion on the defrosting mechanism should be done on the basis of not only the frequency, but also physical details of the 'contact'.

(3) Under the condition of lower surface temperatures, the frost layer becomes dense and hard by particle impingement and is scratched off in the form of a small piece from the tube surface; the defrosting effect by sliding particles weakens on the tube sides. Consequently, the frosted area extends from the tube sides toward the stagnation point and tube top.

(4) The defrosting performance of the present very shallow fluidized bed can be well correlated with the temperature difference between inlet air and tube surface, $(T_{ai} - \bar{T}_w)$, and the jet Reynolds number Re_j in the experimental range of the inlet air temperature of -7 to 5°C and $(T_{ai} - \bar{T}_w) = 4$–14 K. Thus, frost-free running is maintained if $T_{ai} - \bar{T}_w < 10$ K.

(5) The total heat-transfer coefficients of the cooled tube in frost-free running are higher than those of a heated tube, because of effective utilization of latent heat cooling by frost formation and defrosting. The total heat-transfer coefficients for a frosting tube are much lower than those of a heated tube owing to the thermal resistance of the frost layer.

Acknowledgements—The authors express sincere gratitude to Professors W. Schneider and U. Schaflinger, Institut für Strömungslehre und Wärmeübertragung, Technische Universität Wien, for their useful discussions and suggestions. This work is a part of the research supported by a Grant-in-Air for Scientific Research A-63420029 and a Grant-in-Aid for International Scientific Research Program No. 06044018 from the Ministry of Education, Science, and Culture of Japan.

REFERENCES

1. Yamakawa, N., Takahashi, N. and Ohtani, S., Forced convection heat and mass transfer under frost condition. *Heat Transfer Japanese Research*, 1972, **1**, 1–10.
2. Hayashi, Y., Aoki, K. and Yuhara, H., Study of frost formation based on a theoretical model of the frost layer. *Heat Transfer Japanese Research*, 1977, **6**, 79–94.
3. Seki, N., Fukusako, S., Matsuo, K. and Uemura, S., An analysis of incipient frost formation. *Wärme- und Stoffübertragung*, 1985, **19**, 9–18.
4. Aoki, K., Hattori, M. and Itoh, T., A study of extended surface heat exchanger with frosting (1st report, overall heat transfer characteristics), *Transactions of the JSME, Series B*, 1985, **51**, 3048–3054 (in Japanese).
5. Ohara, T., Aihara, T., Kitano, H. and Shimoyama, T., Heat transfer of a horizontal array of frosted tubes in impinging jets. *Transactions of the Society of Air-Conditioning and Sanitary Engineering of Japan*, 1995, **58**, 103–109 (in Japanese).
6. Grewal, N. S. and Saxena, S. C., Heat transfer between a horizontal tube and a gas–solid fluidized bed, *International Journal of Heat and Mass Transfer*, 1980, **23**, 1505–1519.
7. Borodulya, V. A., Ganzha, V. L., Podberezsky, A. I., Upadhyay, S. N. and Saxena, S. C., Heat transfer between fluidized beds of large particles and horizontal tube bundles at high pressures, *International Journal of Heat and Mass Transfer*, 1984, **27**, 1219–1225.
8. George, S. E. and Grace, J. R., Heat transfer to horizontal tubes in the freeboard region of a gas fluidized bed. *AIChE Journal*, 1982, **28**, 759–765.
9. Biyikli S., Tuzla, K. and Chen, J. C., Heat transfer around a horizontal tube in freeboard region of fluidized beds. *AIChE Journal*, 1983, **29**, 712–716.
10. Nagahashi, Y. and Hirayama, N., Heat transfer from a horizontal cylinder surface immersed in fluidized bed (maximum heat-transfer coefficient and optimum velocity). *Transactions of the JSME, Series B*, 1983, **49**, 2163–2171 (in Japanese).
11. Fukusako, S., Ishiguro, S. and Seki, N., Heat-transfer characteristics from a bundle of horizontal tubes immersed in aggregative fluidized bed. *Wärme- und Stoffübertragung*, 1985, **22**, 13–22.
12. Kurosaki, Y., Ishiguro, H. and Takahashi, K., Fluidization and heat-transfer characteristics around a horizontal heated circular cylinder immersed in a gas fluidized bed. *International Journal of Heat and Mass Transfer*, 1988, **31**, 349–358.
13. Ishiguro, H., Kurosaki, Y. and Yasui, M., A fundamental study of fluidization and heat transfer characteristics around a horizontal heated circular cylinder immersed in a fluidized bed (2nd report, effect of the properties of the particles and the device for promoting heat transfer). *Transactions of the JSME, Series B*, 1990, **56**, 1733–1740 (in Japanese).
14. Kurosaki, Y., Satoh, I. and Ishize, T., Mechanisms of heat transfer enhancement for fluidized-bed-type heat exchangers (estimation of direct-contact heat exchange from a heat transfer surface to fluidized particles by an optical visualization technique. *Transactions of the JSME, Series B*, 1991, **57**, 3128–3135 (in Japanese).
15. Ishiguro, H., Ichikawa, K. and Nariai, H., Unsteady fluidization structure and heat transfer mechanism around a horizontal heated circular cylinder in a gas fluidized bed. In *Proceedings of the Third ASME/JSME Thermal Engineering Joint Conference*, Kino, Vol. 4, 1991, pp. 513–520.
16. Fukusako, S., Tago, M., Yamada, M., Ozaki, M., Torikoshi, K. and Kawabata, K., Frosting heat transfer from a bundle of horizontal tubes immersed in aggregative fluidized bed. In *Heat Transfer With Phase Change*, ASME HTD Vol. 114, ed. Habib, I. S. and Dallman, R. J. ASME, New York, 1989, pp. 29–37.
17. Torikoshi, K., Kawabata, K. and Yamashita, H., Heat transfer from a tube immersed in a fluidized bed with frosting. *Heat Transfer Japanese Research*, 1990, **19**, 73–91.
18. Aihara, T., Maruyama, S., Hongoh, M. and Aya, S., Heat transfer and pressure loss of a very shallow fluidized-bed heat exchanger, Part 1, experiment with a single row of tubes. *Experimental Thermal and Fluid Science*, 1988, **1**, 315–323.
19. Maruyama, S., Aihara, T., Tanaka, Y. and Kasahara, K., Heat transfer and pressure loss of a very shallow fluidized-bed heat exchanger, Part 2, experiment with multirow tube banks. *Experimental Thermal and Fluid Science*, 1988, **1**, 325–333.
20. Maruyama, S., Aihara, T., Tanaka, Y. and Kasahara, K., Development of an air-cooled bare-tube condenser utilizing low pressure-loss fluidized bed for heat-pump systems. *Transactions of the Society of Air-Conditioning and Sanitary Engineering of Japan*, 1989, **40**, 57–63 (in Japanese).
21. Aihara, T., Gakumazawa, H., Maruyama, S. and Hongoh, M., Frost formation and defrosting on tube-array evaporators in a fluidized bed and an impinging jet. *Experimental Thermal and Fluid Science*, 1989, **2**, 65–71.
22. Katoh, Y., Miyamoto, M., Chimura, T. and Idei, Y., The study on particle behavior in the expansion of fluidized bed using a simple optical probe. *Transactions of the JSME, Series B*, 1991, **57**, 3244–3247 (in Japanese).
23. Watanabe, Y., Morikawa, T., Kumada, M. and Mabuchi, I., Flow and heat-transfer characteristics around tube banks in floating particles. In *Proceedings of the 24th National Heat Transfer Symposium*, Matsuyama, 1987, pp. 145–147 (in Japanese).
24. Schaflinger, U., Aihara, T., Gruber, T., Weingerl, U., Ohara, T. and Schneider, W., Analysis of particle motion in a very shallow fluidized bed. *Journal of Multiphase Flow* (in press).
25. Kumada, M., Mabuchi, I. and Kawashima, Y., Mass transfer on a cylinder in the potential core region of a two-dimensional jet. *Heat Transfer Japanese Research*, 1973, **2**, 53–66.
26. Kumada, M., Mabuchi, I., Kawashima, Y. and Hirata, M., Mass transfer on a cylinder in developed region of a two-dimensional jet. *Heat Transfer Japanese Research*, 1976, **5**, 1–13.